A Passive High-Temperature High-Pressure Solar Steam Generator for Medical Sterilization

A passive high-temperature high-pressure solar steam generator for medical sterilization

Lin Zhao[1], Bikram Bhatia[1], Lenan Zhang[1], Elise Strobach[1], Arny Leroy[1], Manoj K. Yadav[2], Sungwoo Yang[1], Thomas A. Cooper[1], Lee A. Weinstein[1], Anish Modi[2], Shireesh B. Kedare[2], Gang Chen[1], and Evelyn N. Wang[1*]

[1]*Department of Mechanical Engineering, Massachusetts Institute of Technology, Cambridge, MA 02139, USA*
[2]*Deptartment of Energy Science and Engineering, Indian Institute of Technology Bombay, Powai, Mumbai 400076, Maharashtra, India*

Summary

Saturated steam (>121 °C and >205 kPa) is widely used in the medical sterilization process known as autoclaving. However, solar-driven steam generation at such high temperature and pressure requires expensive optical concentrators. We demonstrate a passive solar thermal device mostly built from low-cost off-the-shelf components capable of delivering saturated and pressurized steam to drive sterilization cycles even under hazy and partly cloudy weather. Enabled by an optimized ultra-transparent silica aerogel, the device utilizes an efficient thermal concentration strategy to locally increase the heat flux and temperature obviating the need for active optical concentrators. With more than 2x higher energy efficiency (56%) than those previously reported at 100 °C, the device demonstrated successful sterilization in a field test performed in Mumbai, India. In addition to enabling passive sterilization, this work promises the development of solar thermal energy systems for saturated steam generation in energy conversion, storage, and transport applications.

Keywords

Solar thermal energy, steam generation, aerogel, sterilization, thermal concentration

*enwang@mit.edu

Introduction

Health care-associated infection (HCAI) represents the most frequent adverse medical events especially in developing countries. According to a recent report published by the World Health Organization, more than 19% of patients are affected by HCAI in low- and middle-income countries, resulting in increased antimicrobial resistance, nearly 30% higher mortality rates for critical patients, prolonged hospital stays up to weeks, and massive cost burden for the health care systems and the patients.[1,2] Besides implementing standard precautions and promoting awareness, a critical step in alleviating this challenge is ensuring proper sterilization of invasive medical equipment. The most effective and widely adopted procedure to sterilize medical equipment and materials is known as autoclaving, where saturated steam at elevated temperature and pressure (>121 °C and >205 kPa or 2.05 bar) condenses and rapidly releases its latent heat to destroy the infectious agents.[3] Compared with other heat-based sterilization methods, the autoclaving process leverages the large latent heat of water to achieve effective sterilization in a short period (≈ 30 mins). However, in order to generate the required saturated steam, commercially available autoclaves rely on either electricity or fuel which is inaccessible to many resource-limited regions, resulting in higher infection rates.[1]

Recent developments in small-scale solar-driven technology have enabled utilization of the abundant solar energy for water vapor generation in remote areas.[4–11] Leveraging interfacial solar heat localization, improved thermal design, and enthalpy recycling, substantially higher solar-to-vapor conversion efficiencies have been reported.[12–18] However, these high efficiency systems typically operate at relatively low temperatures (<50 °C), which are insufficient for medical sterilization. Although high-temperature solar steam generation has been demonstrated in recent studies, their solar-to-steam conversion efficiency is limited (≈ 20%) due to higher heat losses at elevated temperatures (>100 °C).[19–22] Therefore, new strategies are required to enable efficient solar steam generation processes at high temperatures.

Realizing high-efficiency high-temperature solar steam generation in a small-scale system is a critical technological challenge that could enable novel applications of solar thermal energy systems. A common way to generate saturated steam is through boiling when rapid liquid-to-vapor phase change takes place. For water at atmospheric pressure, the minimum heat flux at the onset of nucleate boiling is about 7 kW/m^2 – seven times higher than the peak solar irradiance on Earth ≈1 kW/m^2.[23,24] This substantial energy flux mismatch necessitates the use of active optical concentrators (10-1000x), similar to those used in large-scale solar thermal plants, to boil water with sunlight.[25–27] An optical concentrator focuses the incoming solar radiation to an absorber, as shown in Figure 1A (left), increasing its temperature and heat flux beyond the boiling threshold to initiate steam generation. However, the cost and complexity of bulky optical concentrators and associated tracking systems have prevented widespread adoption of solar steam generation, especially in remote and resource-limited areas.

An alternative and simpler approach to locally increasing the temperature and heat flux is via thermal concentration. Here a larger solar absorbing surface converts sunlight to heat and conducts the heat to a smaller area, thereby increasing the heat flux to enable steam generation as shown in Figure 1A (right). The thermal concentration approach relies on heat conduction that can be easily realized using low-cost thermally conducting materials (*e.g.,* metals) without any moving parts.[28] Thermal concentration is already implemented in many existing solar thermal systems using a tube-fin solar absorber (Figure 1B), where a thin metallic fin absorbs solar radiation and concentrates heat towards the tube through the small fin thickness.[29] However, when compared with the optical approach, the additional heat loss due to (1) the larger absorber surface area and (2) the temperature gradient along the absorber (Figure 1A, middle panel) severely deteriorates the thermal concentration performance at elevated temperatures. The efficiency of thermal concentration, *i.e.,* the ratio of the concentrated thermal energy to the total incoming solar energy $\eta_{th} = Q_{\text{heat}}/Q_{\text{solar}}$, strongly depends on the base temperature of the absorber fin T_b and the heat loss coefficient h as shown in Figure 1C. When h approaches 10 W m^{-2} K^{-1} (typical for open systems in air), the energy efficiency quickly drops to below 20% for T_b = 100 °C, especially when the input solar flux is lower than 1 kW/m^2 due to atmospheric conditions and cosine loss (see supplemental note 1 for detailed thermal analysis). This result is consistent with recent studies that demonstrate saturated steam generation at 100 °C using >1000x thermal concertation but achieve energy efficiency ≈ 20%.[19,21] Due to this challenge, state-of-the-art steam generation at sterilization conditions (>121 °C and >205 kPa) still relies on optical concentration with active tracking despite the system complexity and cost.[30–33]

In this work, we present a passive solar thermal device that can generate saturated steam at the required sterilization conditions even under partly cloudy and hazy skies without any moving parts. Enabled by an optimized silica aerogel layer, the device uses an off-the-shelf tube-fin solar absorber to reach the required temperature and heat flux via thermal concentration. In order to overcome the heat loss limitation, optically transparent and thermally insulating silica aerogel tiles were fabricated and integrated into the device to reduce the effective heat loss coefficient h to about 1 W m^{-2} K^{-1} – a 10x suppression compared to typical open solar vapor systems. This extremely low heat loss allows the thermal concentration process to be as efficient as the optical concentration counterpart (Figure 1C). In a field test performed in Mumbai, India

(19° 7′ 48″ N, 72° 55′ 8″ E), the device generated saturated steam at 100 °C with 56% efficiency (solar flux ≈ 0.7 kW/m^2) – more than 2x higher than the highest-reported efficiency achieved in a controlled laboratory environment with constant 1 sun illumination.[19,20] In addition to the highly efficient thermal concentration process, the planar absorber geometry facilitates the use of a simple non-tracking compound-parabolic concentrator (CPC) to further increase the power capacity of the device at the expense of a small efficiency drop to 47%. Enabled by the high energy efficiency, the sterilization process at 128 °C and 250 kPa was successfully demonstrated and verified using a standard autoclave indicator tape. This work provides a new low-cost pathway to generate saturated steam with natural sunlight, which could help alleviate avoidable infections in resource-limited regions and facilitate the adoption of solar thermal technology in applications such as power generation and industrial process heat.

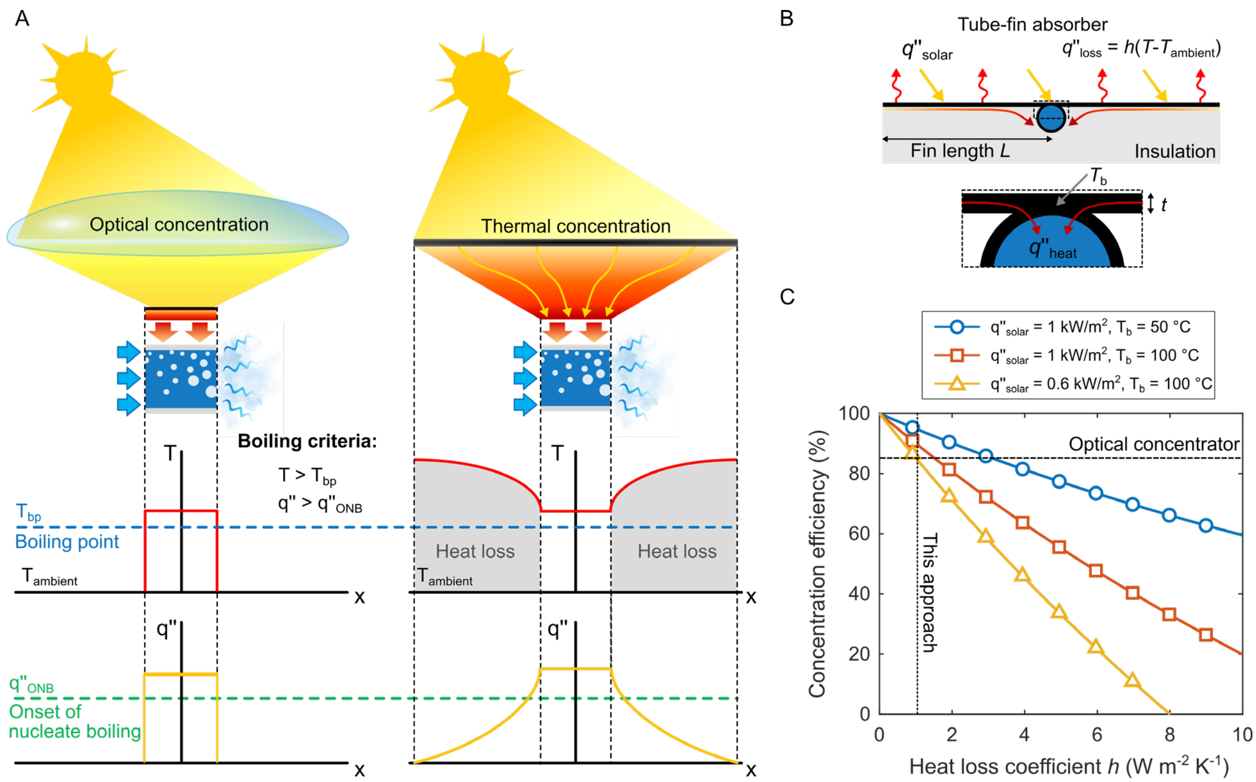

Figure 1. Thermal concentration enabled saturated steam generation. (**A**) Increasing local heat flux by optical (left) and thermal (right) concentration. To initiate nucleate boiling of water, the surface temperature must be higher than the boiling point T_{bp} (wall superheat) and the local heat flux needs to surpass the value at the onset of nucleate boiling q''_{ONB}. The middle and bottom panel illustrate the corresponding temperature and heat flux distribution along the solar absorber surface for optical and thermal concentration. The shaded area in the temperature distribution of thermal approach indicates the additional heat loss due to the enlarged absorber area. (**B**) Schematic of a typical tube-fin solar absorber. (**C**) Thermal concentration efficiency as a function of the surface heat loss coefficient h for different solar flux and base temperatures. The horizontal dashed line shows the performance of a typical optical concentrator and the vertical dashed line shows the comparable thermal concentration performance achieved in this work. (see supplemental note 1 for detailed thermal analysis)

Results

The design and construction of the steam generator prototype is shown in Figure 2. A tube-fin absorber (Thermafin Manufacturing, 127 mm × 965 mm) made of copper with a selective solar absorbing coating was used for its high solar absorptance, low infrared emittance, and high thermal conductivity. The backside of the absorber was insulated by a 50 mm thick fiberglass sheet. The absorber was enclosed in a protective aluminum enclosure and the top aperture was covered by a sheet of borosilicate glass (Swift Glass, 3.3 mm thick). Ten transparent aerogel tiles (150 mm × 100 mm × 7 mm) were placed on top of the absorber surface in place of the air gap in conventional solar collectors. A non-tracking CPC with a geometric concentration ratio of 2.13x (acceptance angle = 25°) was fabricated by bending two pieces of thin aluminum mirrors into a parabolic shape. The CPC provides a simple way to increase the input solar power without active diurnal tracking.[34] Additionally, because of the low concentration ratio, the CPC is also able to harness a fraction of the diffuse solar radiation which is beneficial for operation during cloudy and hazy weather conditions.

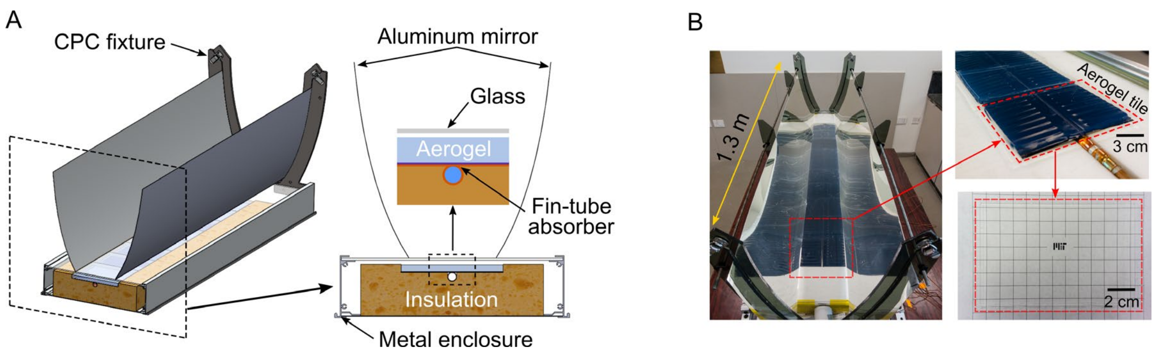

Figure 2. Design and fabrication of the steam generator prototype. (**A**) CAD schematic and (**B**) photograph of the assembled prototype. An aluminum enclosure was built to house the fin-tube solar absorber and fiberglass insulation was used to reduce the backside heat loss. Ten monolithic transparent aerogel samples were tiled to cover the entire solar absorbing surface (red-dashed box in **B**). The non-tracking CPC was constructed by bending two aluminum mirrors into the designed parabolic shape, which were held by plastic fixtures.

Optimization of optical and thermal transport in the steam generator prototype enables efficient thermal concentration. First, solar radiation is captured and absorbed with minimal loss. As shown in Figure 3A, the high solar transmittance of the silica aerogel and glass in combination with the high reflectance of the concentrator mirror ensures that the majority of incident solar radiation reaches the absorber and is converted into heat. Unlike conventional translucent silica aerogel,[35–39] we have recently shown it is possible to achieve ultra-high solar transmittance (≈ 95%) by optimizing the microstructure of the aerogel to reduce scattering.[40–44] The low scattering coefficient, *i.e.*, longer photon mean free path, is especially beneficial when solar radiation is incident from oblique angles due to the diurnal movement of the sun and atmosphere scattering from clouds and particulate matter (see supplemental note 2 for aerogel characterization details). To quantify the optical effect of adding the aerogel layer, we performed ray tracing simulations (Figure 3B) which showed that the additional aerogel layer had a minimal impact (≈ 5%) on the system's optical efficiency (see supplemental note 3 for ray tracing details). Specifically, within the acceptance angle of the CPC, the optical efficiency is over 80% for beam radiation and over 32% for diffuse radiation with the aerogel layer present. Second, the optimized silica aerogel significantly suppresses the heat loss from the absorber surface as depicted in Figure 3C. The aerogel's inherent porous structure with pores (≈ 20 nm average diameter) smaller than the air mean free path (≈ 70 nm) and tortuous backbone reduces the gas- and solid-phase heat transfer. The high extinction in the infrared spectrum (Figure 3A) diminishes radiative heat transfer within the aerogel, which becomes the dominant heat transfer mode at elevated temperatures (>100 °C).[45] Additionally, the selective absorber further reduces the radiation loss by imposing a low-emissivity boundary condition on the aerogel especially in the spectral range where the blackbody spectrum starts to overlap with the transparent window of the aerogel in the 3-5 μm wavelength range (Figure 3A).

To fully leverage the benefit of the aerogel, its thickness needs to be carefully chosen to balance the gain in thermal insulation and the loss in optical transmittance. As the aerogel thickness increases, the solar transmittance deteriorates while the thermal insulation improves. The optimal thickness depends on the operating conditions such as absorber temperature and solar radiation flux. Figure 3D illustrates the trend of optical and thermal loss as a function of the aerogel thickness for two representative solar fluxes (1, 2 kW/m^2) at 100 °C. For both cases, the total energy loss quickly decreases with increasing aerogel thickness at small aerogel thicknesses (< 5 mm). When the aerogel thickness is greater than 10 mm, the total energy loss starts to level and eventually increase due to the dominance of optical losses. This trade-off results in an optimal aerogel thickness range of 6 - 9 mm which represents the most favorable balance between optical and thermal loss. Therefore, we used 7 mm thick aerogel tiles in the prototype. The optimized aerogel was a key feature that enabled the prototype – otherwise built from off-the-shelf components – to be a high-performance solar steam generator capable of achieving temperatures and pressures required for sterilization without relying on complicated optical systems or expensive infrastructure.

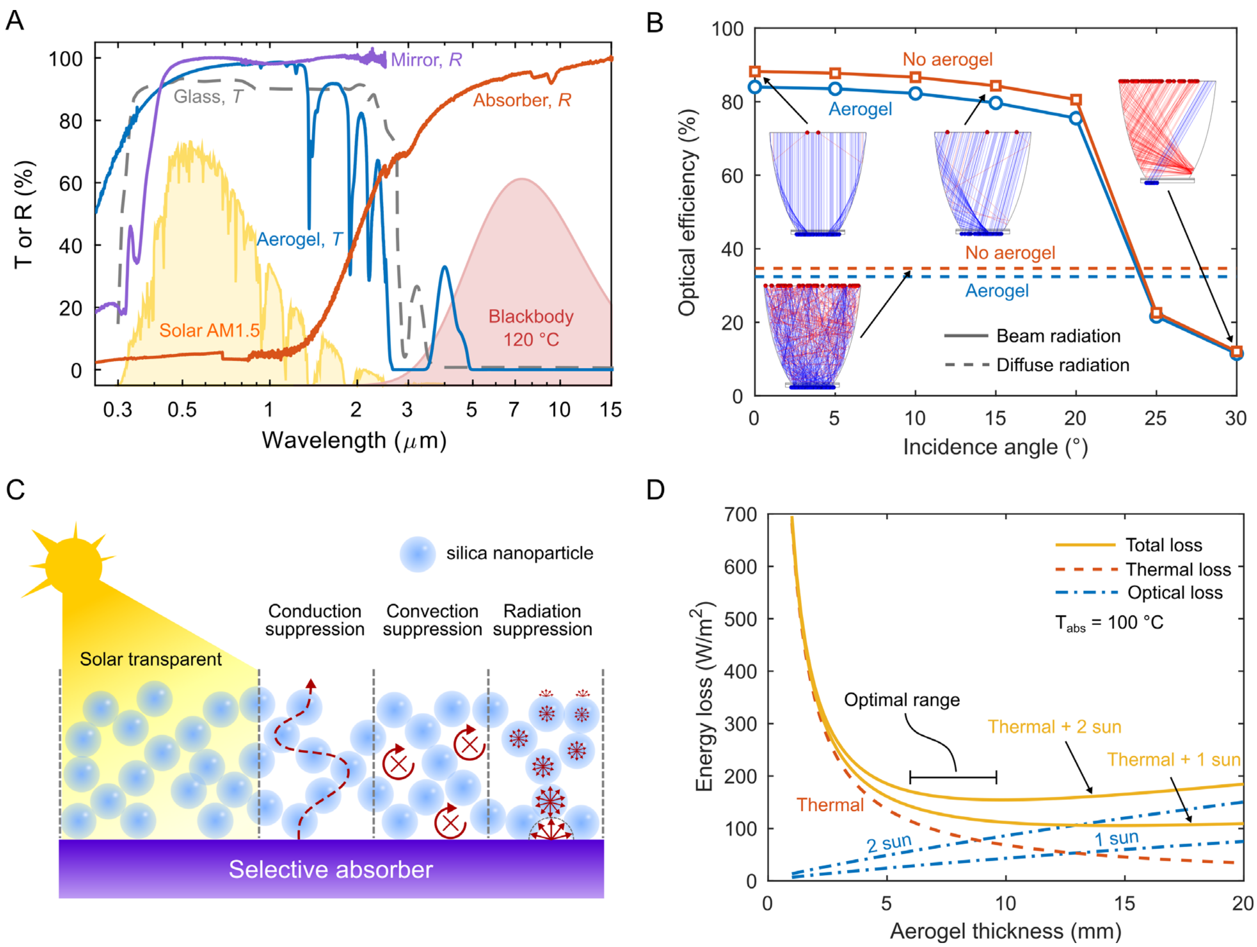

Figure 3. Optical and thermal properties of prototype components. (**A**) Transmittance (T) and reflectance (R) spectra of the aerogel, absorber, glass, and mirror in the solar and infrared region. (**B**) Ray tracing results for both collimated beam radiation and diffuse radiation. The optical efficiency is defined as the ratio of the incident solar flux intercepted by the CPC aperture and the flux absorbed by the absorber. Inset: snapshots of the ray path (blue trajectory - ray that reaches the solar absorber, red trajectory - ray that misses the absorber). Because of the aerogel's high transparency in the solar spectrum, it has a minimal impact (≈ 5%) on the overall optical efficiency at the designed thickness. (**C**) Schematic of the aerogel optical and thermal characteristics. The aerogel is transparent to solar radiation because of the ultra-small particle size and the lack of intrinsic absorption of silica in the solar spectrum. Meanwhile, the tortuous particle backbone, nanometer-size pores, and high infrared extinction suppress heat transfer via conduction, convection, and radiation. (**D**) Optical, thermal, and total energy loss as a function of aerogel thickness for input solar flux of 1 and 2 kW/m^2 and absorber temperature of 100 °C.

To evaluate the prototype performance under realistic weather conditions, we performed steam generation and sterilization demonstrations in Mumbai, India as a representative field test location in the developing world. The experiments were conducted on the rooftop of the Department of Energy Science and Engineering building in the campus of Indian Institute of Technology Bombay (IITB). In the first set of experiments, we investigated the steam generation rate at 100 °C under atmospheric pressure. As shown in

Figure 4A, the experimental loop consists of the steam generator prototype, with the inlet connected to a water tank and the outlet open to the atmosphere. The water tank was placed on a mass balance (SJX6201N/E, Ohaus) to monitor its weight change with time. After filling with water, the water tank opening was capped, ensuring negligible dark evaporation contribution. By setting the water tank at an appropriate height, water was continuously driven into the prototype by gravity and maintain a constant water level (≈ 2/3 full) in the prototype. Thermocouples located at the inlet (T_1), the middle (T_2, T_4, T_5), the outlet (T_3), and the steam vent (T_{steam}) of the prototype were attached to monitor the internal temperature of the prototype and an extra thermocouple (shielded from direct sunlight) was used to measure the ambient temperature. A pyranometer (LP-02, Hukseflux) was placed near the prototype to measure the global horizontal solar irradiance (GHI). All the measurements were recorded by a data acquisition module (34972A, Agilent) connected to a computer. Figure 4B shows a photograph of the prototype during the experiment. The prototype was aligned towards the south and tilted at 40° to match the zenith angle of the sun at solar noon. Figures 4C-E show the temperature evolution, GHI, and mass change during the experiment, respectively. The experiment started around 11:30 (solar time) when the ambient temperature and humidity were around 29 °C and 53%. Shortly after the start, we exposed the prototype to sunlight which begun heating. Within 10 minutes into the experiment, the steam vent temperature abruptly increased to 100 °C indicating the onset of steam generation. The temperature spike at the prototype outlet (T_3) was due to the initial dryout, which was then stabilized at 100 °C after a steady flow of steam was established (Figure 4C). Despite the low incident solar flux (≈ 0.65 kW/m^2) due to hazy weather conditions, constant steam generation was maintained throughout the experiment (≈ 1 hour) as shown by the steady steam temperature at 100 °C. The fin edge temperatures were about 15 °C higher than the center of the absorber ($T_{4,5}$ versus T_2) to establish the temperature gradient necessary to thermally concentrate the heat flux from the fin edge to the tube.

The performance of the prototype can be quantified by the steam generation rate and energy efficiency. We calculated the steam generation rate when the prototype reached a quasi-steady-state from 12:00 to 12:10 and the energy efficiency can be quantified as

$$\eta = \frac{\dot{m}\left(h_{fg} + c_p \Delta T\right)}{CAq"_{\text{solar}}} \approx \frac{\dot{m} h_{fg}}{CAq"_{\text{solar}}} \times 100\% \qquad (1)$$

where $\dot{m}$ is the steam generation rate estimated from the slope of the mass change data, h_{fg} is the enthalpy of water vaporization, $c_p\Delta T$ is the sensible heat contribution (c_p – heat capacity, ΔT – temperature rise from the water inlet temperature to boiling temperature), C is the optical concentration ratio, A is the absorber area (m^2), and $q"_{\text{solar}}$ (kW/m^2) is the average solar flux incident at the prototype aperture (converted from

GHI based on the orientation of the prototype aperture). In this calculation, we used h_{fg} = 2,257 kJ/kg corresponding to the latent heat at 100 °C and excluded the sensible heat contribution to be conservative. To quantify the performance enhancement due to the aerogel and CPC, we performed additional experiments on three consecutive days with the aerogel tiles removed, the CPC removed, and both the aerogel tiles and the CPC removed from the prototype (see details of the additional experiments in supplemental note 4). The energy efficiency of each case is shown in Figure 4F. Comparing results of the experiments with and without aerogel tiles, we observed a >2x energy efficiency enhancement – achieving the highest efficiency of 56% for the "aerogel only" case followed by 47% for the "aerogel + CPC" case. The corresponding volumetric steam generation rates are 2.5 L/min (aerogel only) and 4.2 L/min (aerogel + CPC). The reduced efficiency with the CPC was due to the additional optical loss. This demonstrated performance under realistic weather conditions with ≈ 0.65 kW/m^2 solar flux represents a significant improvement from previous results (efficiency ≈ 20%) under controlled lab environment and illustrates the effectiveness of an optimized system using thermal concentration for solar steam generation.

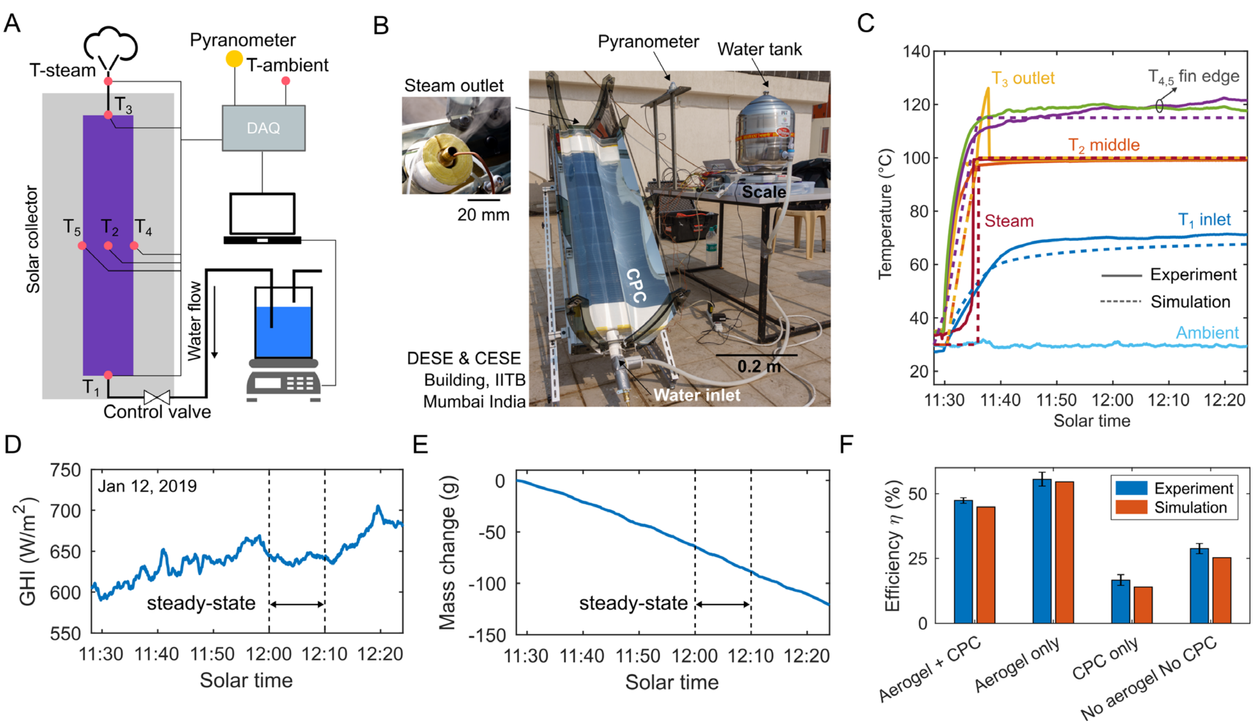

Figure 4. Steam generation performance at 100 °C. (**A**) Schematic of the experimental setup. (**B**) Photograph of the experiment performed on Jan 12, 2019 at IITB campus. (**C**) Temperature response of various components of the prototype during the experiment. Simulated temperature evolution is shown as dashed lines for comparison. (**D**) Measured GHI and (**E**) mass loss during the experiment. (**F**) Measured and simulated energy efficiency of the prototype for four experimental configurations: (1) with aerogel tiles and CPC, (2) aerogel tiles without CPC, (3) CPC without aerogel tiles, and (4) without aerogel tiles and CPC.

To fully understand the optical and thermal transport in the prototype, we also developed a numerical model that can capture the transient and steady-state behavior of the experimental setup. The model takes the prototype configuration, material properties, and weather conditions as inputs and predicts the temperature evolution as well as the energy efficiency of the steam generation process. The influence of atmospheric conditions on the total solar energy incident on the prototype was incorporated in the model via the sky clearness index which includes the effects of both clouds and particulate matters in the sky. As shown in Figures 4C and 4F, the simulation results are in good agreement with the experimental measurements. The small deviations are likely due to the uncertainties in experimental measurements and simplifications in the model (see modeling details in supplemental note 5). Nevertheless, the developed model can guide system design for a variety of applications and enable system performance optimization under different operating conditions.

To study the sterilization performance, we modified the prototype by connecting a closed chamber to the steam vent (Figure 5A). A pressure relief valve (Z000207, All American) was attached to the chamber to maintain a constant pressure at ≈ 250 kPa. The pressure and temperature of the chamber were monitored by a pressure sensor (PX309-030G5V, Omega Engineering) and a thermocouple probe. A piece of standard autoclave indicator tape (Lead Free Autoclave Steam Indicator Tape, 3M) was attached to the surface of the thermocouple probe. The autoclave tape is designed to show a dark stripe after exposed to the required sterilization temperature and pressure conditions for a sufficient amount of time. It is worth noting that maintaining the required steam conditions (>121 °C and >205 kPa) for at least 30 minutes is critical to realize effective sterilization of all common bacteria and microorganisms, as suggested by the Centers for Disease Control and Prevention.[3] Although steam at lower temperatures can also kill bacteria, it requires a much longer time to deliver the same Sterility Assurance Level (SAL). For example, to achieve equivalent microbial lethality, it would require 80 hours with steam at 100 °C but only requires 12 minutes at 121 °C.[46,47] With continuous measurement of the temperature and pressure in the chamber, we can ensure sufficient steam exposure time at the required conditions is achieved. In addition, the autoclave tape as a commonly used chemical indicator serves as a secondary assurance.

Before the experiment, water was filled to the top of the absorber tube to ensure sufficient water for the entire experiment. After filling, the control valve was closed to prevent water back flow due to pressurization. The pressure relief valve attached to the chamber was left open at the beginning of the experiment. The chamber pressure and temperature evolution as well as GHI are shown in Figure 5B. The experiment started at around 11:45 and within 5 minutes boiling started, as indicated by the abrupt temperature increase measured by the chamber temperature probe (labeled as “Onset of boiling” in Figure 5B). Shortly after the chamber temperature reached 100 °C, we closed the pressure relief valve to allow both the temperature and pressure to build up (labeled as “Pressurization” in Figure 5B). The chamber pressure increased quickly and eventually stabilized at 250 kPa (setpoint of the pressure relief valve) and the chamber temperature reached 128 °C. To achieve effective sterilization, it is critical to create a pure saturation environment and prevent any air pockets inside the chamber. Therefore, we followed the standard procedure[3] by opening the pressure relief valve to vent the chamber before the sterilization process as shown by the drop in pressure and temperature to 100 kPa and 100 °C at 12:08 (labeled as “Air vent” in Figure 5B). The actual sterilization process started at around 12:10 when we closed the pressure relief valve again. The chamber pressure and temperature recovered quickly and stabilized at 250 kPa and 128 °C. The sterilization conditions were maintained continuously for 30 minutes (12:14 to 12:44) despite the fluctuating and less-than-ideal solar flux (≈ 0.7 kW/m^2). After the sterilization was completed, we opened the chamber and examined the autoclave tape. As shown in Figure 5C, the dark stripe appeared after the process, indicating successful realization of the sterilization cycle.

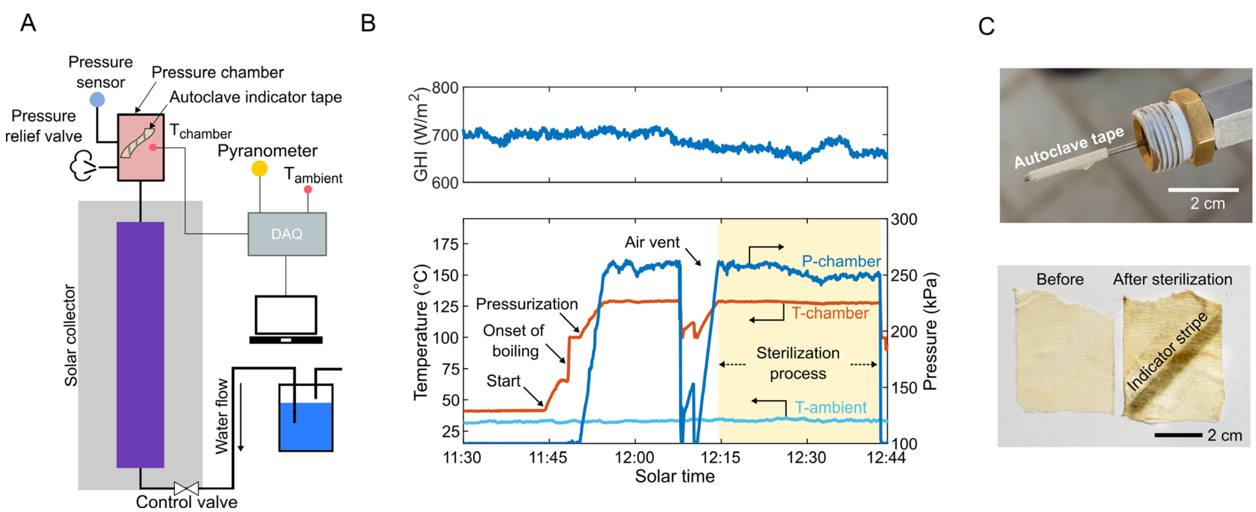

Figure 5. Sterilization demonstration. (**A**) Schematic of the experimental setup for the sterilization demonstration. A pressure chamber was connected to the steam outlet of the collector and a pressure relief value regulates the chamber pressure at ≈ 250 kPa. (**B**) Chamber pressure, temperature, and GHI during the experiment. The yellow shaded region indicates the effective autoclaving period. (**C**) Verification of effective sterilization – comparing a piece of the autoclave indicator tape before (left) and after (right) the sterilization process.

Discussion

To show the significance of the demonstrated thermal concentration approach, we compare our work with recent studies on solar steam generation. The results are presented in Figure 6 with the input solar flux as the *x*-axis and output steam temperature as the *y*-axis. The results space can be divided into four quadrants delineated by solar flux = 10 suns and steam temperature = 100 °C. As shown in Figure 6, a majority of the studies occupy quadrants I and III, roughly following a linear relationship between input solar flux and steam temperature. The intersection point (10 suns, 100 °C) indicates approximately a 10x optical concentration is necessary to generate steam over 100 °C in these studies. Therefore, to achieve sterilization with pressurization, previous systems require high optical concentration ratios (>10x), represented by the filled symbols in quadrant I. More recently, efforts have been focused on reducing the required optical concentration using low-cost efficient thermal designs. A few studies have shown the possibility to further boost the steam temperature via a subsequent superheating stage (open symbols in quadrant II).[20,32,48] However, due to the relatively low efficiency, pressurized saturated steam generation beyond 100 °C was only available in quadrant I in previous research. Enabled by the highly efficient thermal concentration approach, this work provides a viable solution for generating saturated and pressurized steam – represented by the filled star in quadrant II. As a stationary and passive device built from widely available low-cost components, the total estimated cost of the prototype is approximately $38 (0.26 m^2 aperture area) including the solar absorber, glass, CPC, fiberglass insulation, enclosure, and silica aerogel (see cost analysis details in supplemental note 6). With a nominal solar input of 260 W, 3-6 units of the prototype will be sufficient to power a benchtop autoclave, illustrating its potential to alleviate the infection burden in remote and developing regions of the world.

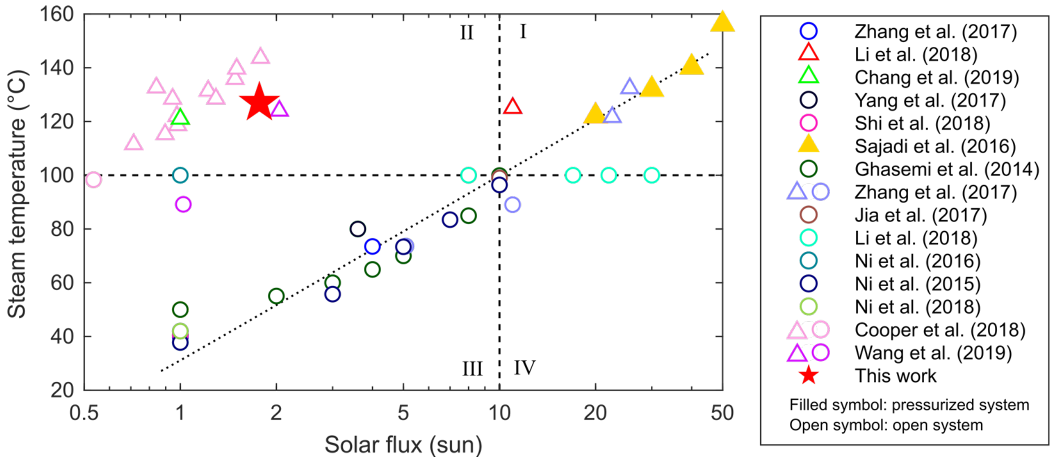

Figure 6. Comparison of the measured steam temperature as a function of input solar flux reported in the literature. Circles and triangles represent steam generation temperatures below and above the water boiling point (100 °C), respectively. Filled and open symbols represent steam generation in pressurized systems and open systems, respectively. To achieve high steam temperatures and pressurization, previous studies relied on high solar flux indicated by the dotted line in quadrants I and III.[12,15,19,31,33,49–55] A few recent studies employed a subsequent superheating stage to boost the steam temperature beyond 100 °C in open systems (open symbols in quadrant II).[20,32,48] This work demonstrates that it is possible to generate saturated and pressurized steam with low optical concentration represented by the only filled symbol in quadrant II.

In conclusion, we show that by using a thermal concentration approach and optimizing the optical and thermal design, high efficiency saturated steam generation beyond 100 °C can be achieved using a simple passive low-cost device without any moving parts even under partially haze and cloudy atmospheric conditions. Enabled by the ultra-transparent and thermally insulating silica aerogel, a prototype device built mostly from off-the-shelf components can generate saturated steam at 100 °C with 56% efficiency under realistic weather conditions – more than two times higher than previously reported results in well-controlled laboratory environments. When connected to a pressure chamber, the prototype can continuously deliver pressurized steam at 128 °C and 250 kPa, sufficient for driving the medical sterilization cycle. As reliable access to energy sources does not exist in many remote and resource-limited regions, conventional electrical- or fuel-powered autoclaves cannot operate effectively. Therefore, the low-cost passive solar-powered autoclaves similar to the one demonstrated in this work could help relieve health care-related infection burden in those areas. The same design and optimization principle can also be applied to other systems that require saturated steam such as power generation and industrial processes – representing an exciting opportunity to promote solar thermal energy.

Experimental Procedures

Materials

Silica aerogel monoliths were synthesized by sol-gel polymerization of tetramethyl orthosilicate (TMOS, 131903, Sigma-Aldrich) in a methanol solution, catalyzed by ammonia (NH_3, 2.0 M in Methanol, 341428, Sigma-Aldrich) to promote both hydrolysis and condensation reactions. The mixing molar ratio of chemicals was NH_3 : TMOS : water : methanol = 0.0348:1:4:6.42. The solution was poured into a disposable polystyrene container (150 mm × 100 mm) with a target thickness of 7 mm. The solution gelled in the container within about 2 minutes and was then allowed to age in the air-tight container. After 2 weeks, the aged gel was taken out of the container for drying. The mother solvent was replaced with ethanol (EtOH, 89234−848, VWR) for critical point drying (CPD, model 931, Tousimis) with liquid CO_2. After drying, the monolithic aerogels were annealed at 200 °C for 24 h to remove water and any organic residue.

Compound parabolic concentrator (CPC) fabrication

The designed shape of the CPC mirror was transferred to an acrylic fixture (thickness = 0.25 inch) using high-precision laser cutting (Epilog Laser). The fixture had two separate pieces that were clamped along with the aluminum mirror to define its shape. Rubber strips (width = 0.25 inch, McMaster-Carr) were attached to the contacting surfaces of the fixture to ensure uniform clamping force on the mirror. For each mirror, two fixtures were used at each end. A support structure was added in the middle to reduce mirror warping. The assembled CPC was then attached to the prototype enclosure by mounting screws. See supplemental note 7 for CPC construction details.

Optical characterization

The optical properties of the aerogel, solar absorber, glass pane, and the mirror were characterized using a UV-vis-NIR spectrophotometer (Cary 5000, Agilent) with an integrating sphere (Internal DRA-2500, Agilent) in the solar spectrum and a Fourier transform infrared (FTIR) spectrometer (Nicolet 5700) with a Pike Technologies mid-IR integrating sphere in the infrared spectrum.

Supplemental Information

Supplemental information includes 7 figures and 4 tables can be found with this article online at

Author Contributions

L. Zhao and B. B. designed the experiments with inputs from all authors. L. Zhang, A. L., and L. Zhao developed the numerical heat and mass transfer model. L. Zhao, B. B., and M. K. Y. conducted the field test. E. S., S. Y., and L. Zhao optimized and prepared the aerogel samples. E. S. and B. B. measured the optical properties. T. A. C., L. A. W., and L. Zhao designed the ray tracing study and interpreted the results. L. Zhao, B. B., and L. Zhang wrote the manuscript with inputs from all authors. A. M., S. B. K., G. C., and E. N. W. guided the overall project.

Acknowledgments

L. Zhao gratefully acknowledges the graduate fellowship from the MIT Tata Center for Technology + Design. This work made use of experimental facilities that are a part of the Solid-State Solar Thermal Energy Conversion (S3TEC) Center, an Energy Frontier Research Center funded by the US Department of Energy, Office of Science, Basic Energy Sciences under Award Number DE-FG02-09ER46577 (optical characterization). M. K. Y., A. M., and S. B. K. gratefully acknowledge the financial support by the Tata Centre for Technology and Design, IIT Bombay. L. Zhao thanks Qihui Qian, Dr. Angeliki Diane Rigos, Dr. Jason Prapas, Dr. Robert Stoner, and Dr. Chintan Vaishnav for their generous help in this project.

Reference

1. World Health Organisation, and Organisation, W.H. (2011). Report on the burden of endemic health care-associated infection worldwide: Clean care is safer care.

2. Allegranzi, B., Nejad, S.B., Combescure, C., Graafmans, W., Attar, H., Donaldson, L., and Pittet, D. (2011). Burden of endemic health-care-associated infection in developing countries: Systematic review and meta-analysis. Lancet *377*, 228–241.

3. Steam Sterilization Guideline for Disinfection and Sterilization in Healthcare Facilities (2008) https://www.cdc.gov/infectioncontrol/guidelines/disinfection/sterilization/steam.html.

4. Chen, C., Kuang, Y., and Hu, L. (2019). Challenges and Opportunities for Solar Evaporation. Joule *3*, 683–718.

5. Tao, P., Ni, G., Song, C., Shang, W., Wu, J., Zhu, J., Chen, G., and Deng, T. (2018). Solar-driven interfacial evaporation. Nat. Energy *3*, 1031–1041.

6. Pang, Y., Zhang, J., Ma, R., Qu, Z., Lee, E., and Luo, T. (2020). Solar–Thermal Water Evaporation: A Review. ACS Energy Lett. *5*, 437–456.

7. Zhao, F., Guo, Y., Zhou, X., Shi, W., and Yu, G. (2020). Materials for solar-powered water evaporation. Nat. Rev. Mater. *5*, 388–401.

8. Zhang, C., Liang, H., Xu, Z., and Wang, Z. (2019). Harnessing Solar-Driven Photothermal Effect toward the Water–Energy Nexus. Adv. Sci. *6*, 1900883.

9. Alvarez, P.J.J., Chan, C.K., Elimelech, M., Halas, N.J., and Villagrán, D. (2018). Emerging opportunities for nanotechnology to enhance water security. Nat. Nanotechnol. *13*, 634–641.

10. Boriskina, S. V., Raza, A., Zhang, T., Wang, P., Zhou, L., and Zhu, J. (2019). Nanomaterials for the water-energy nexus. MRS Bull. *44*, 59–66.

11. Zhou, J., Gu, Y., Liu, P., Wang, P., Miao, L., Liu, J., Wei, A., Mu, X., Li, J., and Zhu, J. (2019). Development and Evolution of the System Structure for Highly Efficient Solar Steam Generation from Zero to Three Dimensions. Adv. Funct. Mater. *29*, 1903255.

12. Ghasemi, H., Ni, G., Marconnet, A.M., Loomis, J., Yerci, S., Miljkovic, N., and Chen, G. (2014). Solar steam generation by heat localization. Nat. Commun. *5*, 4449.

13. Zhou, L., Tan, Y., Wang, J., Xu, W., Yuan, Y., Cai, W., Zhu, S., and Zhu, J. (2016). 3D self-assembly of aluminium nanoparticles for plasmon-enhanced solar desalination. Nat. Photonics *10*,

393–398.

14. Zhao, F., Zhou, X., Shi, Y., Alexander, M., Mendez, S., Qu, L., Qian, X., Alexander, M., Zhao, X., Mendez, S., et al. (2018). Highly efficient solar vapor generation via hierarchically nanostructured gels. Nat. Nanotechnol. *13*, 489–495.

15. Jia, C., Li, Y., Yang, Z., Chen, G., Yao, Y., Jiang, F., Kuang, Y., Pastel, G., Xie, H., Yang, B., et al. (2017). Rich Mesostructures Derived from Natural Woods for Solar Steam Generation. Joule *1*, 588–599.

16. Menon, A.K., Haechler, I., Kaur, S., Lubner, S., and Prasher, R.S. (2020). Enhanced solar evaporation using a photo-thermal umbrella for wastewater management. Nat. Sustain., 35–43.

17. Zhang, L., Xu, Z., Bhatia, B., Li, B., Zhao, L., and Wang, E.N. (2020). Modeling and performance analysis of high-efficiency thermally-localized multistage solar stills. Appl. Energy *266*, 114864.

18. Xu, Z., Zhang, L., Zhao, L., Li, B., Bhatia, B., Wang, C., Wilke, K.L., Song, Y., Labban, O., Lienhard, J.H., et al. (2020). Ultrahigh-efficiency desalination via a thermally-localized multistage solar still. Energy Environ. Sci. *13*, 830–839.

19. Ni, G., Li, G., Boriskina, S.V. V., Li, H., Yang, W., Zhang, T.J., and Chen, G. (2016). Steam generation under one sun enabled by a floating structure with thermal concentration. Nat. Energy *1*, 16126.

20. Cooper, T.A., Zandavi, S.H., Ni, G.W., Tsurimaki, Y., Huang, Y., Boriskina, S. V., and Chen, G. (2018). Contactless steam generation and superheating under one sun illumination. Nat. Commun. *9*.

21. Liang, J., Ji, X., Han, J., and Wang, Y. (2020). Modeling and experimental investigation on a direct steam generation solar collector with flat plate thermal concentration. Energy Explor. Exploit., 014459872092268.

22. Zhang, L., Zhao, L., and Wang, E.N. (2020). Stefan flow induced natural convection suppression on high-flux evaporators. Int. Commun. Heat Mass Transf. *110*, 104255.

23. Cheng, P., Quan, X., Gong, S., Liu, X., and Yang, L. (2014). Recent Analytical and Numerical Studies on Phase-Change Heat Transfer. Adv. Heat Transf. *46*, 187–248.

24. Mills, A.F. (1999). Heat Transfer 2nd ed. (Prentice Hall).

25. Weinstein, L.A., Loomis, J., Bhatia, B., Bierman, D.M., Wang, E.N., and Chen, G. (2015).

Concentrating Solar Power. Chem. Rev. *115*, 12797–12838.

26. Hirsch, T., Feldhoff, J.F., Hennecke, K., and Pitz-Paal, R. (2014). Advancements in the Field of Direct Steam Generation in Linear Solar Concentrators—A Review. Heat Transf. Eng. *35*, 258–271.

27. Zarza, E., Valenzuela, L., León, J., Hennecke, K., Eck, M., Weyers, H.-D., and Eickhoff, M. (2004). Direct steam generation in parabolic troughs: Final results and conclusions of the DISS project. Energy *29*, 635–644.

28. Kraemer, D., Poudel, B., Feng, H., Caylor, J.C., Yu, B., Yan, X., Ma, Y., Wang, X., Wang, D., Muto, A., et al. (2011). High-performance flat-panel solar thermoelectric generators with high thermal concentration. Nat. Mater. *10*, 532–538.

29. Duffie, J.A., and Beckman, W.A. (2013). Solar Engineering of Thermal Processes (John Wiley & Sons, Inc.).

30. Neumann, O., Feronti, C., Neumann, A.D., Dong, A., Schell, K., Lu, B., Kim, E., Quinn, M., Thompson, S., Grady, N., et al. (2013). Compact solar autoclave based on steam generation using broadband light-harvesting nanoparticles. Proc. Natl. Acad. Sci. *110*, 11677–11681.

31. Sajadi, S.M., Farokhnia, N., Irajizad, P., Hasnain, M., and Ghasemi, H. (2016). Flexible artificially-networked structure for ambient/high pressure solar steam generation. J. Mater. Chem. A *4*, 4700–4705.

32. Wang, X., Liu, Y., Feng, R., Zhang, Y., Chang, C., Fu, B., Luan, T., Tao, P., Shang, W., Wu, J., et al. (2019). Solar-driven high-temperature steam generation at ambient pressure. Prog. Nat. Sci. Mater. Int. *29*, 10–15.

33. Li, J., Du, M., Lv, G., Zhou, L., Li, X., Bertoluzzi, L., Liu, C., Zhu, S., and Zhu, J. (2018). Interfacial Solar Steam Generation Enables Fast-Responsive, Energy-Efficient, and Low-Cost Off-Grid Sterilization. Adv. Mater. *30*, 1–7.

34. Spirkl, W., Ries, H., Muschaweck, J., and Winston, R. (1998). Nontracking solar concentrators. Sol. Energy *62*, 113–120.

35. Günay, A.A., Kim, H., Nagarajan, N., Lopez, M., Kantharaj, R., Alsaati, A., Marconnet, A., Lenert, A., and Miljkovic, N. (2018). Optically Transparent Thermally Insulating Silica Aerogels for Solar Thermal Insulation. ACS Appl. Mater. Interfaces *10*, 12603–12611.

36. Pajonk, G.M. (1998). Transparent silica aerogels. J. Non. Cryst. Solids *225*, 307–314.

37. Buratti, C., and Moretti, E. (2012). Glazing systems with silica aerogel for energy savings in buildings. Appl. Energy *98*, 396–403.

38. McEnaney, K., Weinstein, L., Kraemer, D., Ghasemi, H., and Chen, G. (2017). Aerogel-based solar thermal receivers. Nano Energy *40*, 180–186.

39. Weinstein, L.A., McEnaney, K., Strobach, E., Yang, S., Bhatia, B., Zhao, L., Huang, Y., Loomis, J., Cao, F., Boriskina, S. V., et al. (2018). A Hybrid Electric and Thermal Solar Receiver. Joule *2*, 962–975.

40. Zhao, L., Bhatia, B., Yang, S., Strobach, E., Weinstein, L.A., Cooper, T.A., Chen, G., and Wang, E.N. (2019). Harnessing Heat beyond 200 °c from Unconcentrated Sunlight with Nonevacuated Transparent Aerogels. ACS Nano *13*, 7508–7516.

41. Strobach, E., Bhatia, B., Yang, S., Zhao, L., and Wang, E.N. (2017). High Temperature Annealing for Structural Optimization of Silica Aerogels in Solar Thermal Applications. J. Non. Cryst. Solids *462*, 72–77.

42. Strobach, E., Bhatia, B., Yang, S., Zhao, L., and Wang, E.N. (2019). High temperature stability of transparent silica aerogels for solar thermal applications. APL Mater. *7*, 081104.

43. Zhao, L., Strobach, E., Bhatia, B., Yang, S., Leroy, A., Zhang, L., and Wang, E.N. (2019). Theoretical and experimental investigation of haze in transparent aerogels. Opt. Express *27*, A39.

44. Zhao, L., Yang, S., Bhatia, B., Strobach, E., and Wang, E.N. (2016). Modeling silica aerogel optical performance by determining its radiative properties. AIP Adv. *6*, 025123.

45. Heinemann, U., Caps, R., and Fricke, J. (1996). Radiation-conduction interaction: an investigation on silica aerogels. Int. J. Heat Mass Transf. *39*, 2115–2130.

46. de Magalhães Brito, L.F., and Magagna, D. (2004). Sanitation. In Clinical Engineering Handbook (Elsevier), pp. 532–546.

47. Dion, M., and Parker, W. (2013). Steam sterilization principles. Pharm. Eng. *33*, 60–69.

48. Chang, C., Tao, P., Xu, J., Fu, B., Song, C., Wu, J., Shang, W., and Deng, T. (2019). High-Efficiency Superheated Steam Generation for Portable Sterilization under Ambient Pressure and Low Solar Flux. ACS Appl. Mater. Interfaces *11*, 18466–18474.

49. Zhang, P., Li, J., Lv, L., Zhao, Y., and Qu, L. (2017). Vertically Aligned Graphene Sheets Membrane for Highly Efficient Solar Thermal Generation of Clean Water. ACS Nano *11*, 5087–5093.

50. Zhang, Y., Zhao, D., Yu, F., Yang, C., Lou, J., Liu, Y., Chen, Y., Wang, Z., Tao, P., Shang, W., et al. (2017). Floating rGO-based black membranes for solar driven sterilization. Nanoscale *9*, 19384–19389.

51. Ni, G., Miljkovic, N., Ghasemi, H., Huang, X., Boriskina, S. V., Lin, C. Te, Wang, J., Xu, Y., Rahman, M.M., Zhang, T.J., et al. (2015). Volumetric solar heating of nanofluids for direct vapor generation. Nano Energy *17*, 290–301.

52. Yang, J., Pang, Y., Huang, W., Shaw, S.K., Schiffbauer, J., Pillers, M.A., Mu, X., Luo, S., Zhang, T., Huang, Y., et al. (2017). Functionalized Graphene Enables Highly Efficient Solar Thermal Steam Generation. ACS Nano *11*, 5510–5518.

53. Ni, G., Zandavi, S.H., Javid, S.M., Boriskina, S. V., Cooper, T.A., and Chen, G. (2018). A salt-rejecting floating solar still for low-cost desalination. Energy Environ. Sci. *11*, 1510–1519.

54. Shi, Y., Li, R., Jin, Y., Zhuo, S., Shi, L., Chang, J., Hong, S., Ng, K.C., and Wang, P. (2018). A 3D Photothermal Structure toward Improved Energy Efficiency in Solar Steam Generation. Joule *2*, 1171–1186.

55. Li, X., Min, X., Li, J., Xu, N., Zhu, P., Zhu, B., Zhu, S., and Zhu, J. (2018). Storage and Recycling of Interfacial Solar Steam Enthalpy. Joule *2*, 2477–2484.